© 2015. Published by The Company of Biologists Ltd | Journal of Cell Science (2015) 128, 979–991 doi:10.1242/jcs.161463

RESEARCH ARTICLE

Cavin3 interacts with cavin1 and caveolin1 to increase surface dynamics of caveolae

Jagan Mohan[1], Björn Morén[1], Elin Larsson[1], Mikkel R. Holst[2] and Richard Lundmark[1,2,*]

ABSTRACT

Caveolae are invaginations of the cell surface thought to regulate membrane tension, signalling, adhesion and lipid homeostasis owing to their dynamic behaviour ranging from stable surface association to dynamic rounds of fission and fusion with the plasma membrane. The caveolae coat is generated by oligomerisation of the membrane protein caveolin and the family of cavin proteins. Here, we show that cavin3 (also known as PRKCDBP) is targeted to caveolae by cavin1 (also known as PTRF) where it interacts with the scaffolding domain of caveolin1 and promote caveolae dynamics. We found that the N-terminal region of cavin3 binds a trimer of the cavin1 N-terminus in competition with a homologous cavin2 (also known as SDPR) region, showing that the cavins form distinct subcomplexes through their N-terminal regions. Our data shows that cavin3 is enriched at deeply invaginated caveolae and that loss of cavin3 in cells results in an increase of stable caveolae and a decrease of caveolae that are only present at the membrane for a short time. We propose that cavin3 is recruited to the caveolae coat by cavin1 to interact with caveolin1 and regulate the duration time of caveolae at the plasma membrane.

KEY WORDS: Cavin1, Cavin3, Caveolin1, Caveolae, EHD2

INTRODUCTION

The surface of many cell types are decorated with invaginations of the plasma membrane called caveolae. These structures are thought to play important roles in the control of lipid homeostasis, membrane tension, cell adhesion, signalling and endocytosis (Parton and del Pozo, 2013; Shvets et al., 2014). Although the canonical flask-shaped caveolae are quite uniform in size, around 50–100 nm, a range of flat to semi-budded caveolae have been frequently observed (Fujita et al., 2009). At the surface, individual caveolae of a specific quantum size are in equilibrium with multi-caveolar assemblies (caveolae rosettes) (Razani et al., 2002). The dynamics of these structures in terms of lateral movement and rounds of fission and fusion with the plasma membrane has been shown to vary greatly in cells and among cell types (Parton and del Pozo, 2013). Characterisation of the behaviour of caveolae using total internal reflection fluorescence (TIRF) microscopy, has revealed that there are different populations of caveolae ranging from static caveolae without lateral movement, stable caveolae moving rapidly in the plane of the membrane, endocytosed caveolae and caveolae undergoing short-range cycles of fission and fusion with the plasma membrane (Boucrot et al., 2011; Mundy et al., 2002; Pelkmans and Zerial, 2005). This last 'kiss-and-run' type of behaviour appears to be in balance with stable surface association of caveolae, representing a quantal nature of these invaginations (i.e. they are composed of a fixed number of molecules and can exist in different states) in need of strict control. The dimeric ATPase EH-domain containing 2 (EHD2) forms oligomeric rings around lipid membranes and has been shown to interact with caveolae components and localise to the neck of caveolae to stabilise these structures at the cell surface (Morén et al., 2012; Stoeber et al., 2012). Previously, specific kinases were shown to effect such fission and fusion of caveolae (Pelkmans et al., 2005), and following osmotic shock or mechanic stress, caveolae have been proposed to flatten out or be released from the membrane in order to cope with sudden changes in membrane tension (Nassoy and Lamaze, 2012; Sinha et al., 2011). However, the mechanisms controlling the surface association state of caveolae is largely unknown.

Electron microscopy analysis has revealed striations on the cytosolic surface of caveolae, suggesting that these structures are generated and composed by a filamentous protein coat (Rothberg et al., 1992). The integral membrane protein caveolin1 is though to be part of this coat. Caveolin1 is essential for formation of caveolae in non-muscle cells, and loss of this protein leads to severe lipodystrophy in patients (Razani and Lisanti, 2001). Caveolin1 binds to cholesterol and forms homo-oligomers in the membrane creating these unique lipid domains (Murata et al., 1995). Recently, major advances have been made in our understanding of caveolae integrity and generation through the identification of the cavin coat proteins and regulatory proteins integral to caveolae. In mammalian cells, four different cavins are expressed (cavin1, cavin2, cavin3 and cavin4, also known as PTRF, SDPR, PRKCDBP and MURC, respectively), which form distinct complexes in the cytosol and associate with caveolin to build up the caveolae coat (Bastiani and Parton, 2010; Shvets et al., 2014). Cavin4 is, similar to the caveolin1 homologue caveolin3, specific to muscle cells (Bastiani et al., 2009). The central protein cavin1 is essential for the generation of caveolae in all cells as shown both in cultured cell systems and in mice models (Hill et al., 2008; Liu et al., 2008). Cavin2 has been shown to promote membrane curvature and aid in the invagination of caveolae (Hansen et al., 2009). In mice lacking cavin2, clearly affected shallow caveolae were detected in endothelial cells of certain tissues (Hansen et al., 2013). The role of cavin3 at caveolae is less clear and cavin3-knockout mice

[1]Medical Biochemistry and Biophysics, Laboratory for Molecular Infection Medicine Sweden, Umeå University, 901 87, Umeå, Sweden. [2]Integrative Medical Biology, Umeå University, 901 87, Umeå, Sweden.

*Author for correspondence (richard.lundmark@umu.se)

Received 8 August 2014; Accepted 22 December 2014

Journal of Cell Science (2015) 128, 979–991 doi:10.1242/jcs.161463

show no apparent defect in caveolae biogenesis (Hansen et al., 2013; Liu et al., 2014). Cavin3 was originally characterised as a protein kinase C substrate, and many studies have highlighted the importance of this protein as a tumour suppressor (Bai et al., 2012; Wikman et al., 2012; Xu et al., 2001). Cavin3 localises to both surface-associated caveolae and internalised caveolae, termed cavicles, and has been proposed to influence trafficking of cavicles inside the cell (McMahon et al., 2009).

The caveolae coat can be purified as a detergent-resistant high-molecular-mass complex of around 60–80S composed of caveolins and cavins at a proportional ratio (Hayer et al., 2010; Ludwig et al., 2013). Interestingly, however, the cavins have been shown to form different subcomplexes in different tissues, which might reflect specific modes of action of the cavin coat that are dependent on the precise cavin composition (Hansen et al., 2013). Cavin1 was proposed to form homo-trimers and has been shown to interact and form complexes with either cavin2 or cavin3 in a fixed stoichiometry (Ludwig et al., 2013). The competition between cavin2 and cavin3 for binding to cavin1 suggests that these proteins play distinct regulatory roles in the caveolae coat. In this work, we characterise the protein domains and direct interactions that build up, and determine the stoichiometry of the distinct complexes between cavin1 and cavin3. We show that cavin3 binds to caveolin1 in a cholesterol dependent manner and that integration of cavin3 in the caveolae coat controls the dynamic behaviour of surface-associated caveolae.

RESULTS

The N-terminus of cavin3 interacts with the N-terminus of cavin1

In order to characterise the interactions between cavins, we purified full-length and truncated versions of cavin1, cavin2 and cavin3 as fusion proteins to glutathione S-transferase (GST) or thioredoxin (Trx) (Fig. 1A). Using pulldown experiments we found that cavin1 self-associated and bound to cavin2 and cavin3, as previously suggested (Gambin et al., 2014), but that cavin2 and cavin3 did not interact (Fig. 1B; supplementary material Fig. S1A). To characterise the individual regions of the cavins involved in these interactions, we purified truncated versions of

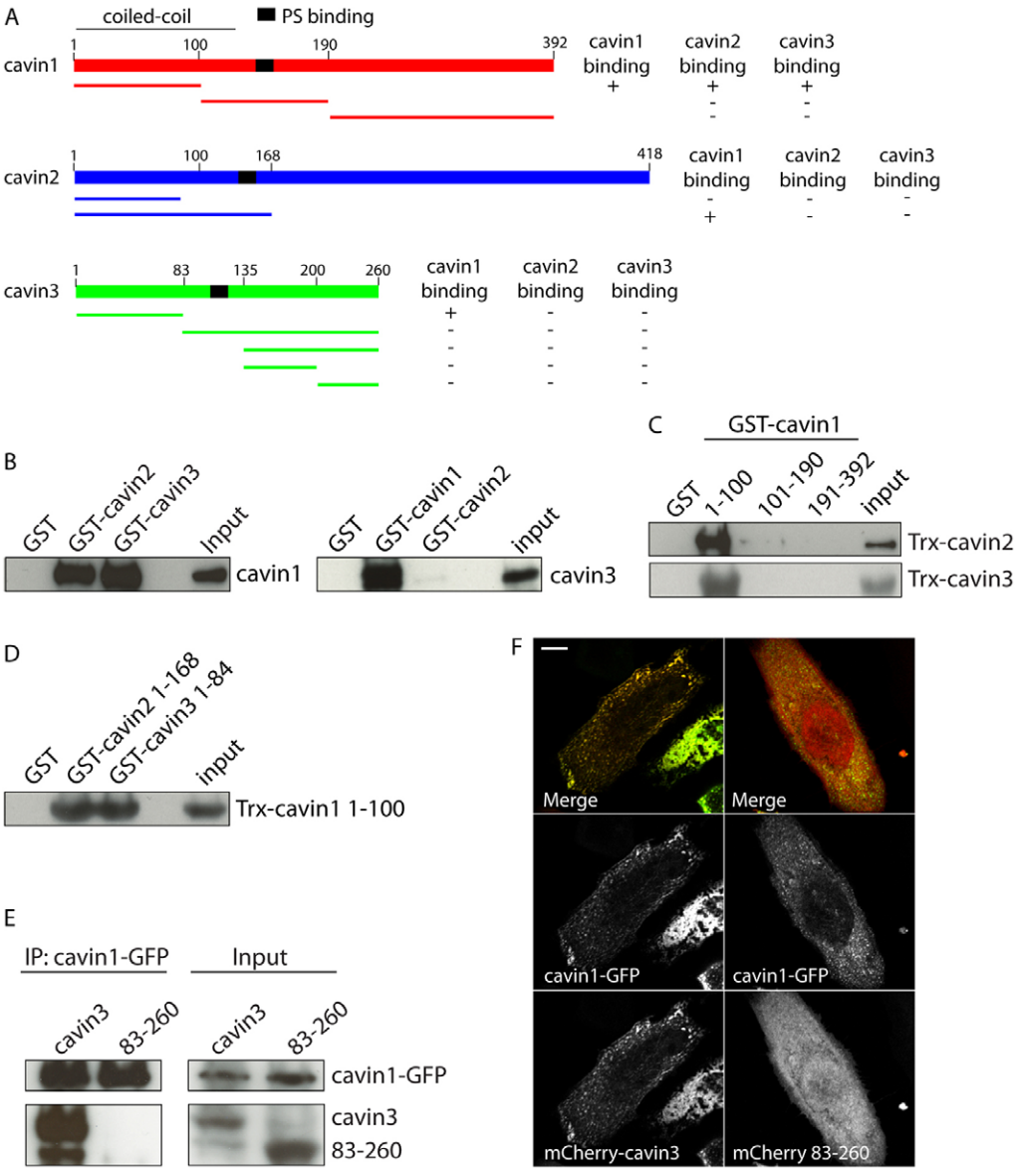

Fig. 1. Cavin3 is recruited to caveolae through an interaction between the N-terminal regions of cavin3 and cavin1. (A) Schematic illustration of the domain organisation of cavin1, cavin2 and cavin3 with the previously proposed phosphatidylserine (PS)-binding sites and the regions involved in interaction among cavin proteins described in this study. (B–D) GST pulldown experiments assaying the binding between the indicated full-length or truncated versions of cavin1, cavin2 and cavin3. (B) Binding between purified full-length cavin1, cavin2 and cavin3, (C) binding between the indicated truncated versions of cavin1 and full-length cavin2 or cavin3, (D) binding between the N-terminal regions of cavin2 (GST–cavin2-1–168) and cavin3 (GST–cavin3-1–84) and cavin1 (cavin1-1–100). Samples were analysed by immunoblotting using antibodies against cavin1, cavin3 or the Trx tag. Purified GST was used as a negative control. (E) Immunoprecipitation (IP) of cavin1–GFP from cells expressing cavin1–GFP together with either mCherry–cavin3 or mCherry–cavin3-83–260. Samples was analysed by immunoblotting using antibodies against GFP and RFP. (F) Confocal images of cells co-expressing cavin1–GFP with either full-length or mCherry–cavin3-83–260. Scale bar: 10 μm.

cavin1, cavin2 and cavin3 for pulldown experiments. The results showed that the N-terminal region of cavin1 (amino acids 1–100) bound to the N-terminal regions of cavin3 (amino acids 1–84) and cavin2 (amino acids 1–168) (Fig. 1C,D; supplementary material Fig. S1B). Surprisingly, the region of cavin3 required for binding (amino acids 1–65) was significantly shorter than the region in cavin2 (amino acids 1–168) (supplementary material Fig. S1C,D). The interaction between cavin1 and the N-terminus of cavin3 was further verified in cells by immunoprecipitation of cavin1–GFP from cells co-expressing cavin1–GFP together with mCherry-tagged cavin3 or cavin3 lacking the N-terminal region. Immunoblotting showed that cavin3, but not cavin3-83–260 was co-immunoprecipitated with cavin1–GFP (Fig. 1E). The N-terminus of cavin3 has previously been reported to be required for targeting of this protein to caveolae. To test whether this was due to the interaction with cavin1, we co-expressed GFP-tagged cavin1 with mCherry-tagged cavin3 or cavin3-83–260 in HeLa cells. We found that the N-terminus was required for colocalisation with cavin1 and caveolin1 and hence caveolae targeting (Fig. 1F). Overexpressed cavin1 and cavin3 colocalised at the membrane in striated structures even in the absence of caveolin1 (supplementary material Fig. S1E), showing that the N-terminal interaction with cavin1 can drive the localisation of cavin3 to membranes, although at endogenous levels, cavins require caveolin for targeting.

Cavin1 forms stable homo-trimers through the N-terminal region

Cavin1 has previously been suggested to self-associate into trimers, and form distinct complexes with cavin2 or cavin3 (Ludwig et al., 2013). Using purified proteins in pulldown experiments, we could show that cavin1 self-associates, but that neither cavin2 nor cavin3 could form homotypic complexes (Fig. 2A). To test if the N-terminus was sufficient to form previously proposed trimers of cavin1, we used glutaraldehyde to crosslink purified Trx–cavin1-1–100 prior to SDS-PAGE analysis. The theoretical molecular mass of Trx–cavin1-1–100 is 25.2 kDa; without crosslinker, cavin1-1–100 migrates as a 30-kDa-sized monomer (Fig. 2B). With increasing amounts of crosslinker, the reduction of monomeric protein was accompanied with the appearance of a protein band at ~90 kDa corresponding to a trimer of cavin1 1–100 (Fig. 2B). We also noticed a weak band around 60 kDa suggesting that a dimer of cavin1 is only partially stable. We next used the gas-phase electrophoretic mobility molecular analyser (GEMMA) technique to analyse the stoichiometry of cavin complexes. When analysing Trx–cavin1-1–100, we identified three peaks corresponding to the molecular mass of 24, 47 and 73 kDa, which nicely match the theoretical molecular mass of a monomer, dimer and trimer of Trx–cavin1, respectively (Fig. 2C). The apparent decrease in the ratio between trimeric and monomeric species observed by GEMMA, compared to crosslinking, reflects the proportional signal reduction obtained by GEMMA and the different buffer conditions used in respective analysis. Similar analysis of Trx–cavin3 constructs revealed that these proteins were not as stable at the lower salt conditions used in GEMMA because a substantial amount of these proteins gave no signal. However, from the peaks matching the individual truncated variants of cavin3 we conclude that the N-terminus of cavin3 is primarily a monomer in solution (supplementary material Fig. S2A,D). Analysis of Trx-tagged cavin1-1–100 by gel filtration revealed that it was present in two distinct peaks (Fig. 2D) corresponding to a globular size of 131.6 kDa (Rs 4.5) and 54.6 kDa (Rs 3.4) as determined by the Stokes radius. Given that these two peaks likely correspond to monomers and trimers, these data suggest that the N-terminus of cavin1 adopts an extended shape leading to a reduced rate of migration through the column. Given that the majority of cavin1-1–100 appears to be present as a trimer in solution, we conclude that the N-terminal region enables the formation of a stable elongated trimeric complex.

Binding of cavin3 to trimeric cavin1 excludes cavin2 from the complex

To characterise the stoichiometry of the cavin3–cavin1 interaction we crosslinked cavin1-1–100 in the absence or presence of increasing amounts of cavin3-1–65, and analysed the samples by SDS-PAGE. The 90-kDa band corresponding to crosslinked trimeric cavin1 was increasingly shifted towards a 130-kDa band following titration of cavin3 (Fig. 2E). The same result was obtained by crosslinking cavin3-1–65 with increasing amounts of cavin1-1–100 (supplementary material Fig. S2E). This suggested that binding of cavin3 to the cavin1 trimers influenced the size or mobility of the cavin complex. To test whether cavin3 bound directly to preformed trimers of cavin1, we crosslinked cavin1 and used cavin3-1–84 as bait in a pulldown assay. Indeed, the results showed that cavin3-1–84 interacted with the stabilised cavin1 trimers (Fig. 2F). This suggests that the N-terminus of cavin3 forms a stable tetrameric complex with a trimer of the N-terminus of cavin1. Because cavin3 and cavin2 have been suggested to form distinct complexes with cavin1 (Gambin et al., 2014; Ludwig et al., 2013), we used the N-terminus of cavin1 to pull down the N-terminal regions of cavin3 or cavin2 proteins under noncompeting or competing conditions. When incubated alone with cavin1, both cavin2 and cavin3 were efficiently pulled down (Fig. 2G). However, when mixed together, we saw a clear reduction in the amount of both cavin3 and cavin2 that interacted with cavin1, showing that cavin2 and cavin3 compete for binding to cavin1 (Fig. 2G,H). Following a preincubation of cavin1 with either cavin2 or cavin3, a further reduction in binding to the competing cavin was observed, indicating that cavin1 adapts to preferentially associate with either cavin2 or cavin3 (Fig. 2G,H). Pull down from preincubated cavin1 and cavin2 shows that cavin3 does not interact with cavin2, although cavin1 was found to bind efficiently to cavin3 (Fig. 2I). The amount of cavin1 pulled down following preincubation with cavin2 again shows that cavin2 and cavin3 are competing for the interaction with cavin1. Our data suggests that cavin2 and cavin3 compete for the same binding site on cavin1 or interact with cavin1 homo-oligomers in different conformations.

The central region of cavin3 binds membranes and interacts with the scaffolding domain of caveolin1 in a cholesterol-dependent manner

Caveolin1 is an integral membrane protein with the N- and C-terminal regions exposed to the cytosol (Fig. 3A) (Williams and Lisanti, 2004). Caveolin1 is known to form oligomers but the way that cavins or cavin complexes interact with caveolin1 is still not known. To test whether cavin1 or cavin3 could directly bind to the N-terminus of caveolin1, we purified truncated caveolin1-1–94 as a GST fusion protein and performed pulldown experiments against cavin1 or cavin3. Strikingly, we detected a clear binding to cavin3 but not cavin1 (Fig. 3B). Using caveolin1-1–94 to pull down truncated versions of cavin3, we could show that the region containing amino acids 135–200 of cavin3 were required to bind to caveolin1 (Fig. 3C). Similarly we used truncated versions of

Journal of Cell Science (2015) 128, 979–991 doi:10.1242/jcs.161463

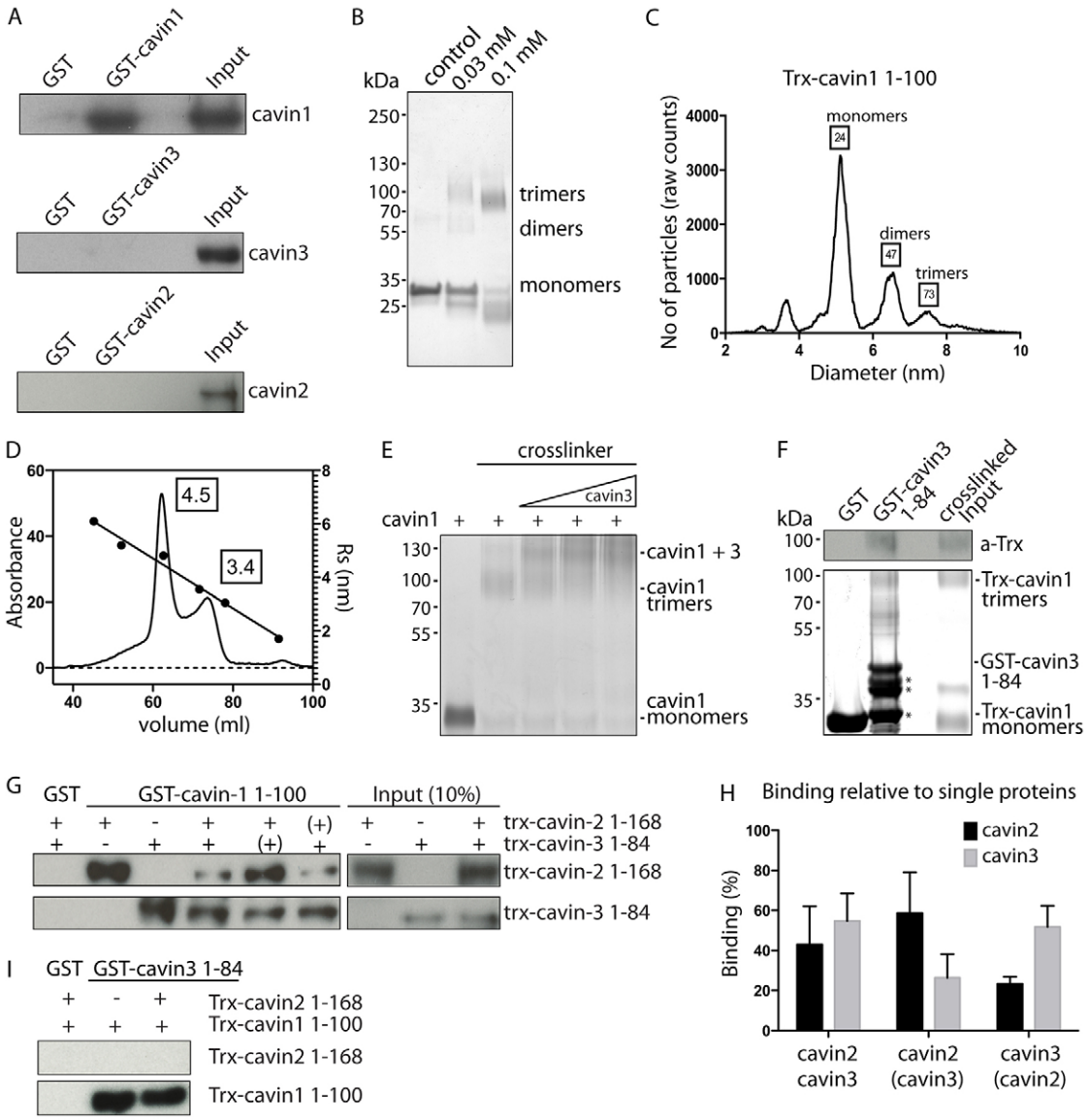

Fig. 2. The N-terminal region of cavin1 forms a stable trimer that associates with either cavin3 or cavin2. (A) GST pulldown analysis of homo-oligomerisation of full-length cavin1, cavin2 and cavin3. GST–cavin1, GST–cavin2 and GST–cavin3 were used as bait against Trx–cavin1, Trx–cavin2 and Trx–cavin3 respectively. GST was used as negative control. Samples were analysed by immunoblotting using anti-Trx antibody. (B) Glutaraldehyde crosslinked Trx–cavin1-1–100 was analysed by a SDS-PAGE followed by Coomassie staining. The control was treated with 1% SDS before analysis. (C) GEMMA analysis of Trx–cavin1-1–100. Each sample was run five times at low pressure to yield reliable data. The *y*-axis shows the protein concentration in particles, entering the detector and *x*-axis shows the particle size in nm. The calculated molecular mass are shown at top of the peak. (D) Gel filtration chromatography of purified Trx–cavin1-1–100. The Stokes radius of two different peaks, 3.4 and 4.5, and, in turn, corresponding molecular masses were estimated based on calibrated standard set of proteins of known Stokes radii. The molecular masses were 54.6 kDa and 131.6 kDa, which correspond to monomers and trimers of Trx–cavin1-1–100. (E) Analysis of glutaraldehyde cros-linked heterocomplex formation by Trx–cavin1-1–100 in the presence of increasing amounts of Trx–cavin3-1–65 by SDS-PAGE followed by Coomassie staining. (F) GST pulldown of cross-linked trimeric Trx–cavin1-1–100 by GST–cavin3-1–84. GST was used as negative control. Samples were analysed by both Coomassie staining and immunoblotting using anti-Trx antibody (a-Trx). *, degraded GST–cavin3-1–84. (G) GST and GST–cavin1-1–100 was incubated with (+) or without (−) Trx–cavin2-1–168 or Trx–cavin3 1–84. '(+)' indicates 5 min preincubation of this protein prior to addition of either Trx-cavin2-1–168 or Trx–cavin3-1–84, respectively. Samples were analysed by immunoblotting using anti-Trx antibodies. (H) Bar graph representing the quantification of binding of cavin2 and cavin3 as determined by experiments performed as in G; the data represents mean±s.d. from three independent experiments. (I) Pulldown experiment showing the binding between the N-terminus of cavin3 (GST–cavin3-1–84) and Trx–cavin1-1–100 alone or Trx–cavin2-1–168 pre-incubated with GST–cavin3-1–84 for 2 h prior to addition of Trx–cavin1-1–100. Samples were analysed by immunoblotting using anti-Trx antibodies.

caveolin1 to show that amino acids 82–94 of caveolin1 were sufficient to bind cavin3 (Fig. 3D). The region 61–101 has been shown to be involved in self-oligomerisation of caveolin1 (Park et al., 2000). To test whether oligomerisation was important for binding to cavin3 we analysed the purified GST-tagged regions of caveolin1 by dynamic light scattering (DLS). The data showed that caveolin1-1–94 formed high mass oligomeres but that further truncation of the protein to amino acids 1–81 resulted in loss of oligomerisation (Fig. 3E). We further verified that untagged caveolin1-1–94 formed oligomers similarly to the GST-tagged protein (Fig. 3E). To test how the interaction between cavin3 and caveolin1 effected the targeting of cavin3 to caveolae, we

Journal of Cell Science (2015) 128, 979–991 doi:10.1242/jcs.161463

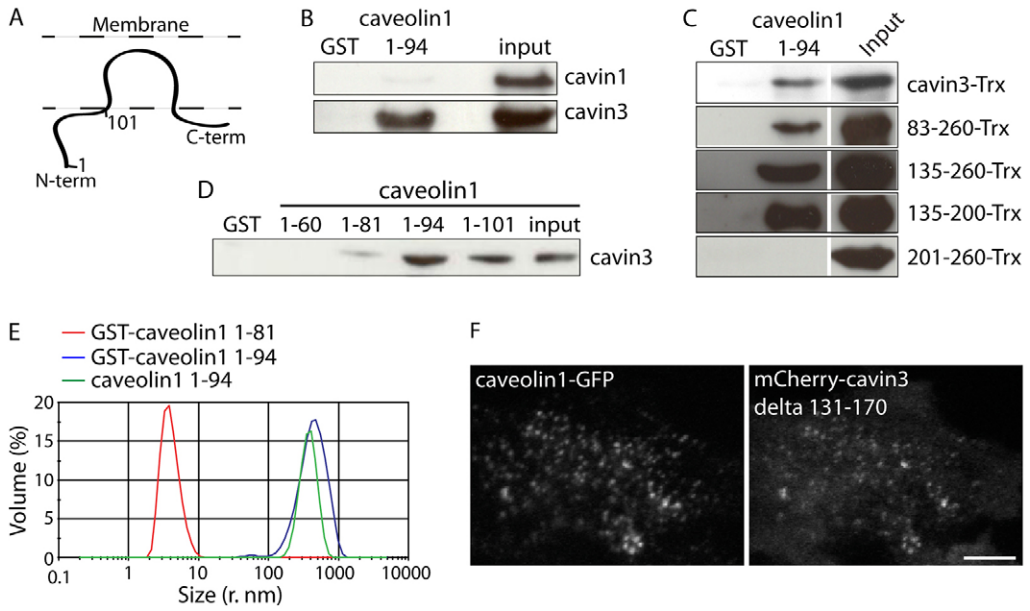

Fig. 3. The middle region of cavin3 binds to the scaffolding domain of caveolin1. (A) Schematic illustration of the assumed positioning of caveolin1 in the membrane. (B) GST pulldown experiment showing the binding between the N-terminus of caveolin1 (GST–caveolin1-1–94) and cavin1 or cavin3. Immunoblots were analysed by anti-cavin1 and anti-cavin3 antibodies, respectively. (C) GST pulldown analysis of binding between Trx-tagged full-length and various truncated forms of cavin3 to GST–caveolin1-1–94. Immunoblots were analysed with anti-Trx antibody. (D) Pulldown analysis of binding between cavin3 and GST-tagged truncated forms of caveolin1 (1–60, 1–81, 1–94 or 1–101). Analysis of the immunoblot was performed with the anti-cavin3 antibody. (E) Diagram showing the dynamic light scattering analysis of GST–caveolin1-1–81, GST–caveolin1-1–94 and caveolin1-1–94. (F) Confocal micrograph of a caveolin1–GFP Flp-In TRex HeLa cell expressing Δ131–170 mCherry–cavin3. Scale bar: 10 μm.

expressed cavin3 or cavin3 lacking the central region (Δ131–170) and imaged the colocalisation with caveolin1. The deletion protein, similar to full-length cavin3, showed extensive colocalisation with caveolin1 (Fig. 3F).

The region 82–101 in caveolin1 has been termed the scaffolding domain owing to its proposed interactions with cholesterol and a variety of different proteins in the cell. The function of the scaffolding domain as a protein-interacting domain has been recently questioned owing to its close proximity to the membrane and the lack of structural consensus in the proposed interaction partners (Byrne et al., 2012; Collins et al., 2012). Given that the scaffolding domain is positioned close to the membrane, we reasoned that the region of cavin3 that binds to the scaffolding domain should be targeted near to the membrane. Using purified proteins in a liposome pulldown assay, we showed that both cavin1 and cavin3 associated with liposomes (Fig. 4A). When we assayed truncated versions of these proteins in the same assay, we found that the central region of both cavin1 (amino acids 101–190) and cavin3 (amino acids 135–200) bound to membranes (Fig. 4B,C). Owing to the high enrichment of cholesterol in caveolae, we assayed whether membrane binding of cavin3 was influenced by the cholesterol content. Indeed, binding was greatly enhanced when the cholesterol levels in the liposomes were elevated, with almost all protein found in the pellet fraction when cholesterol levels were increased by 10% (Fig. 4D). In summary, we conclude that the central region of cavin3 interacts with the scaffolding domain of caveolin1 and cholesterol-enriched membranes. Given that the scaffolding domain also interacts with cholesterol, we analysed whether the binding to cavin3 was sensitive to cholesterol depletion. Caveolin1–GFP was immunoprecipitated from cell lysates following mock treatment or after depletion of cholesterol using methyl-β-cyclodextrin (MβCD) and we used immunoblotting to detect co-immunoprecipitated proteins. Although cavin1 binding was insensitive to cholesterol depletion, the caveolae-stabilising protein EHD2 was completely lost following MβCD treatment (Fig. 4E). Cavin3, by contrast, showed a substantially increased binding to caveolin1 following MβCD treatment (Fig. 4E,F), in agreement with previous results (Breen et al., 2012). In summary, we conclude that the central region of cavin3 interacts with membranes and competes for binding to the scaffolding domain of caveolin1 with cholesterol, but that this binding is not required for targeting of cavin3 to caveolae.

Cavin3 is preferentially associated with deeply invaginated caveolae

The cholesterol-sensitive interaction between cavin3 and the caveolin1 scaffolding domain could potentially influence the induction of membrane curvature by caveolin1 and the budding of caveolae. To be able to determine the size of individual caveolae, we developed a novel technique using correlative atomic force microscopy (AFM) and fluorescence microscopy. We established a stable Flp-In TRex cell line with inducible expression of caveolin1–GFP so that we could use conditions where tagged caveolin1 was present at ~25–50% of the endogenous levels of caveolin1 in order not to induce artificial effects (supplementary material Fig. S3A,B). Caveolin1–GFP-expressing cells grown on cell culture dishes were unroofed, leaving only the ventral plasma membrane attached to the cell culture dish. The surface topography and the fluorescent GFP signal in the membrane were determined using an AFM instrument combined with a fluorescence microscope to allow correlative imaging of the same sample (Fig. 5A). When images were overlaid using software and fluorescent actin filaments as reference points, caveolae marked by caveolin1–GFP could be matched to single peaks in the AFM topography (Fig. 5A,B; supplementary material Fig. S3C). The precise correspondence between fluorescence spots

Journal of Cell Science (2015) 128, 979–991 doi:10.1242/jcs.161463

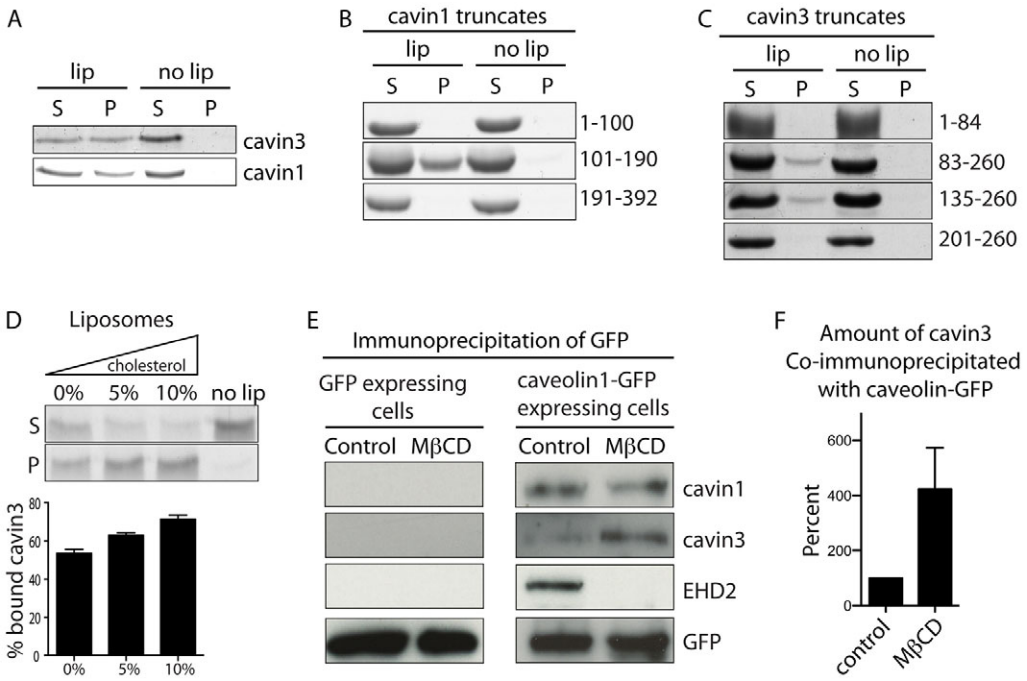

Fig. 4. Membrane binding of cavin3 is cholesterol sensitive and mediated by its middle domain. (A–C) Liposome co-sedimentation assays of (A) full-length cavin1 and cavin3, or (B) truncated versions of cavin1 or (C) cavin3 as indicated. Proteins were incubated with liposomes (lip) or without (no lip) before centrifugation and analysis of supernatant (S) and pellet (P) fractions by SDS-PAGE. (D) Liposome co-sedimentation assay of cavin3 with increasing amount of cholesterol in the liposomes as indicated. Bar graph shows the quantification of pelleted cavin3 representing mean±s.d. from three independent experiments. (E) Immunoprecipitation of GFP-tagged proteins from stable Flp-In TRex cells expressing either caveolin1–GFP or GFP alone following mock treatment (control) or treatment with MβCD to remove cholesterol. Samples were analysed by immunoblotting using antibodies against cavin1, cavin3, EHD2 and GFP. (F) Bar graph showing the quantification of the amount of cavin3 co-immunoprecipitated with caveolin1–GFP in MβCD-treated cells in comparison to control cells as performed in E. The data represents mean±s.d. from three independent experiments.

and AFM peaks verified the methodological approach (Fig. 5A,B). Areas damaged by the unroofing procedure were excluded from the measurements. Using this approach, the heights of caveolin1-positive structures were measured and the quantification showed that the altitude of caveolin1-positive structures ranged from flat to relatively deeply budded (Fig. 5C,D). This verified the previously described variation in caveolae invagination (Hansen et al., 2013; Rothberg et al., 1992). Given that the size of the fluorescent structures also varied (Fig. 5A), these data likely represent single caveolae, clusters and rosetta-like structures.

To test whether cavin3 was associated with a particular type of caveolae, we expressed mCherry–cavin3 in these cells and measured the height of caveolae and their respective signal of mCherry–cavin3. We found that the levels of cavin3 correlated with the depth of invagination of caveolae structures (Fig. 5E,F). The more deeply budded structures had higher levels of cavin3. This indicated that expression of cavin3 either promoted invagination of caveolae or that this protein is recruited to more deeply budded caveolae or caveolae clusters. To test whether cavin3 influences caveolae invagination, we aimed to more precisely measure the altitude of single caveolin1 spots, excluding caveolae clusters, caveolin1 structures located on top of actin filaments and larger caveolin-positive structures. To do this, we used simultaneous expression of caveolin1–GFP and clathrin–mCherry (to mark clathrin-coated pits, as similar-sized reference structures) (Fig. 6A). Fluorescent clathrin punctae were found to precisely correlate with AFM heights in 95% of cases, verifying the methodology. AFM measurement of single caveolin1 and clathrin spots, showed that the average height of such caveolae and clathrin-coated pits was ~25 nm and ~30 nm, respectively (Fig. 6A–C). The size of caveolae has been shown to vary (Fujita et al., 2009; Rothberg et al., 1992), and a recent publication determined that, in tissue sections, the average height of caveolae was around 45 nm (Hansen et al., 2013). The smaller size obtained from our data could be because the more deeply invaginated single caveolae are not stable during the unroofing procedure and in the hypotonic buffer conditions used. This is also likely to influence the deeply budded clathrin-coated pits. Measurement of caveolin1-positive structures in cells depleted of cavin3 showed that there was no difference in the height range or average height compared to control (Fig. 6C). However, analysis of cells expressing mCherry–cavin3 showed that, although the average height of caveolae did not change substantially, higher cavin3 fluorescence intensity correlated with the more deeply budded caveolae (Fig. 6D). Interestingly, we found no correlation between caveolin1 intensity and caveolae height (Fig. 6D), verifying the proposed quantal composition of caveolae (Pelkmans and Zerial, 2005). In summary, we conclude that cavin3 is enriched at more deeply invaginated caveolae structures but that it is not required for the invagination of caveolae, which is in agreement with previous conclusions from cavin3 knock out mice (Hansen et al., 2013; Liu et al., 2014)

Cavin3 and EHD2 control the equilibrium between stable and kiss-and-run types of caveolae at the cell surface

Previous studies in knockout mice have shown that although cavin1 is required to form caveolae and cavin2 contributes to the invagination of caveolae, loss of cavin3 does not seem to affect

Journal of Cell Science (2015) 128, 979–991 doi:10.1242/jcs.161463

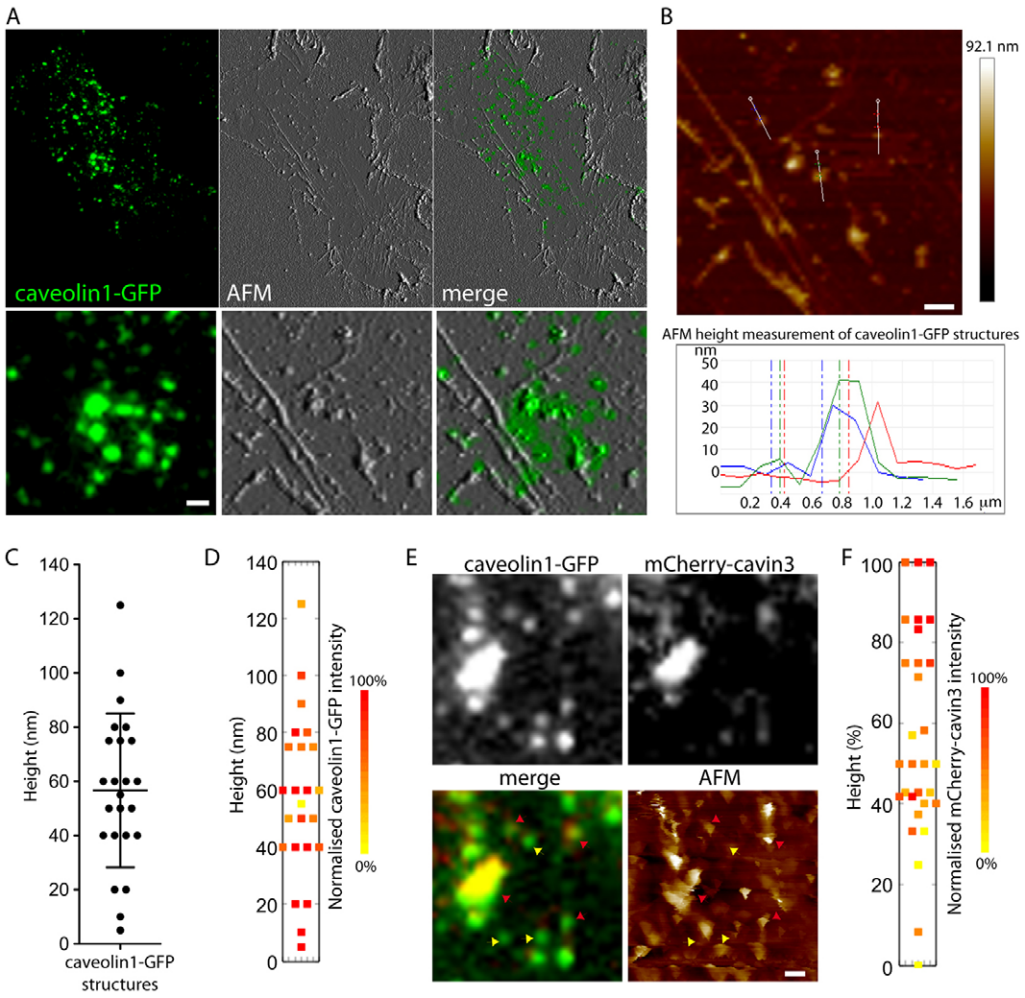

Fig. 5. Cavin3 correlates with larger caveolin1-positive structures. (A) AFM peak force error micrograph overlaid with the correlative caveolin1–GFP intensity as imaged from a representative unroofed HeLa Flp-In TRex cell expressing caveolin1–GFP. Lower images show a magnification of the indicated area. (B) Illustration of the AFM height measurement of the magnified area. The top image shows a topology representation of the AFM analysis with lines indicating the measured regions. The diagram below shows the height distribution (nm) along the lines depicted above. (C) Scatter plot showing the height distribution of caveolin1–GFP-positive spots as determined by AFM measurement as in B. The data represents mean±s.d. from three cells from three independent experiments. (D) Height distribution of caveolin1–GFP-positive spots as determined in C, colour-coded for the normalised level of caveolin1–GFP fluorescence intensity. (E) Overlay of fluorescence micrograph and AFM height map in a HeLa Flp-In TRex cell expressing caveolin1–GFP together with mCherry–cavin3. Red and yellow arrowheads indicate spots with high and low cavin3 fluorescence intensity, respectively. (F) Scatter plot showing the relationship between normalised cavin3 intensity (as colour coded) and the height distribution (%) of caveolin1-positive spots measured from HeLa Flp-In TRex cells expressing caveolin1–GFP together with mCherry. Scale bars: 1 µm

caveolae morphology. Our data suggest that cavin3 acts at the later stages of deeply invaginated caveolae and previous studies has suggested that cavin3 effects caveolae trafficking (McMahon et al., 2009). To study whether cavin3 was involved in regulating the dynamics of caveolae at the cell surface, we used live-cell TIRF microscopy to visualise the behaviour of caveolae in caveolin1–GFP Flp-In TRex cells following small interfering RNA (siRNA)-mediated knockdown of cavin3 or EHD2 (Fig. 7A). Both cavin3 and EHD2 were efficiently knocked down in these cells as determined by immunoblotting, and the levels of both proteins decreased following caveolin1 knockdown (Fig. 7B). Caveolin1-positive structures captured by TIRF microscopy were tracked over time using the Imaris software and the duration time (time of visibility) and displacement (distance between the beginning and end of the track) of each caveolae structure were determined (Fig. 7A). The results showed that the average duration time of caveolae was decreased in cells depleted of EHD2, whereas the lateral displacement length was significantly increased (Fig. 7C,D), which nicely corresponds with previous work showing that EHD2 stabilise caveolae at the cell surface (Morén et al., 2012; Stoeber et al., 2012). Interestingly, the mean duration time of caveolae was increased in cells lacking cavin3, whereas the lateral movement was similar to that in control cells (Fig. 7C,D). We noticed that the relative abundance of caveolae that were stable during the entire movie was increased in cavin3-knockdown cells (Fig. 7A).

To further characterise the effect of the cavin3 and EHD2 knockdowns on caveolae stability, we subdivided the caveolae tracks into very fast (0–30 s), fast (30–75 s), medium (75–150 s), slow (150–225 s) and stable (225–300 s) based on their lifetime at the surface (Fig. 7E). This presentation of the data showed that cavin3 knockdown decreased the populations of the very fast

Journal of Cell Science (2015) 128, 979–991 doi:10.1242/jcs.161463

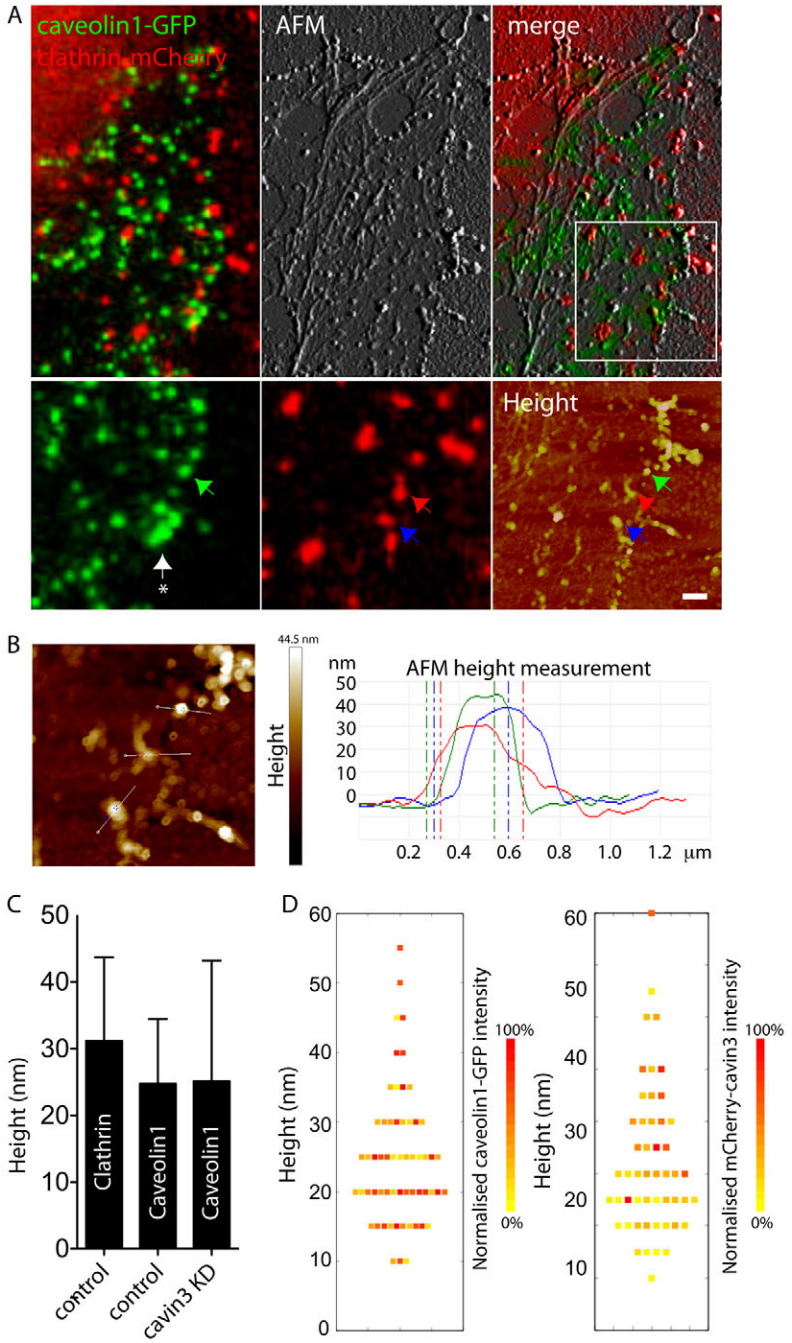

Fig. 6. Cavin3 is enriched at deeply invaginated caveolae. (A) AFM peak force error micrograph overlaid with the correlative fluorescent intensities as imaged from a representative unroofed HeLa Flp-In TRex cell expressing caveolin1–GFP and clathrin–mCherry. Lower images show a magnification of the indicated area. Blue, red and green arrows indicate representative fluorescent structures measured by AFM. The white arrow indicates a representative cluster of caveolae (larger then 500 nm) excluded from the measurement. Scale bars: 1 µm. (B) Topology representation of the AFM analysis with lines indicating the measured regions as indicated by arrows in A. The diagram shows the height distribution (nm) along the lines. (C) Bar graph showing the quantification of the height distribution of caveolin1–GFP-positive spots in control cells and cells depleted of cavin3, and clathrin–mCherry-positive spots in control cells. The data represents mean±s.d. from three cells from three independent experiments. (D) Height distribution of caveolin1–GFP-positive spots colour-coded for the normalised level of caveolin1–GFP and mCherry–cavin3 fluorescence intensity.

caveolae and increased the stable pool of caveolae, and that there was little effect on the other populations (Fig. 7E). Depletion of EHD2, however, resulted in a clear decrease in the relative amount of stable caveolae as expected (Fig. 7E). From this we conclude that cavin3 and EHD2 have opposite effects on the stability of caveolae and the continuous fission and fusion process with the plasma membrane. In order to test whether loss of cavin3 affected EHD2 function, we assayed the localisation and recruitment rate of EHD2 in cells knocked down for cavin3 but found no difference compared to control cells (supplementary material Fig. S4A,B). To determine whether exogenous cavin3 would rescue the phenotype of the knock down, we re-expressed mCherry–cavin3 in cavin3 depleted cells and used TIRF microscopy to track structures positive for both caveolin1–GFP and mCherry–cavin3. The percentage of very fast caveolae was significantly increased compared to cavin3-depleted cells and amplified compared to control cells (Fig. 7E). This effect could not be attributed to an unspecific effect due to the overexpression because only expression of mCherry–cavin3 but not mCherry–cavin2 resulted in the shorter mean duration time of caveolae (Fig. 7F). The influence of cavin3 on caveolae stability seems not to be dependent on the direct interaction with caveolin1 because expression of cavin3-Δ131–170 could also rescue the phenotype following cavin3 depletion (supplementary material Fig. S4D–F). The phenotype whereby there was a greater proportion of dynamic caveolae following EHD2 knockdown could also be reversed by re-expression of exogenous EHD2 (supplementary material Fig. S4C). Taken together, our results show that the

Journal of Cell Science (2015) 128, 979–991 doi:10.1242/jcs.161463

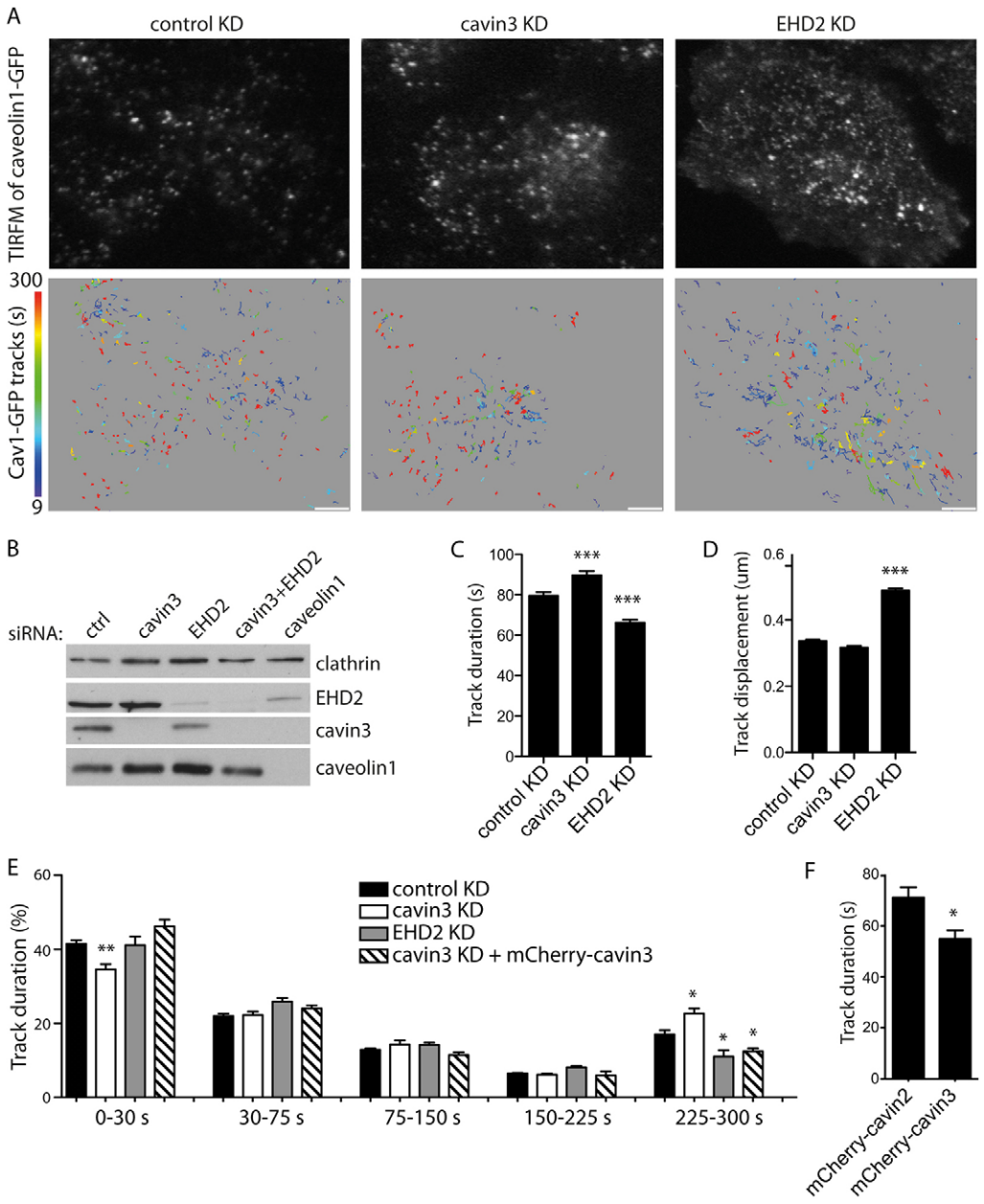

Fig. 7. Depletion of cavin3 in cells increases the extent of caveolae that are stably associated with the cell surface. (A) Representative fluorescence micrographs depicting the start frames from live-cell TIRF microscopy acquisitions of HeLa Flp-In TRex caveolin1–GFP cells transfected with control, cavin3 or EHD2 siRNA. The corresponding caveolin1–GFP structure tracks over time are represented as colour-coded lines. Scale bars: 10 μm. (B) Silencing was confirmed by immunoblotting and detection of the antigens of interest in whole cell lysates. (C) Quantification of track duration of caveolin1–GFP structures (control, $n=1391$), cavin3 ($n=1177$) or EHD2 ($n=999$) from live-cell TIRF microscopy acquisitions of cells transfected with indicated siRNA (knockdown, KD). Error bars represent the s.e.m. from at least five different cells. ***$P<0.0001$ (Student's *t*-test). (D) Quantification of track displacement length of caveolin1–GFP structures from live-cell TIRF microscopy acquisitions of cells transfected with indicated siRNAs, as those in C. (E) Histogram showing distribution of the lifetime of caveolin1–GFP tracks at the plasma membrane in the same cells as in C and in addition with Flp-In TRex caveolin1–GFP cells co-transfected with cavin3 siRNA and mCherry–cavin3. Significance against control KD samples was determined using a two-tailed Mann–Whitney tests. *$P<0.05$, **$P<0.005$ ($n=5$). (F) Quantification of track duration and track displacement length of caveolin1–GFP structures from live-cell TIRF microscopy acquisitions of cells transfected with mCherry–cavin2 or mCherry–cavin3. Error bars represent the s.e.m. from at least four different cells. *$P<0.05$ (Student's *t*-test).

equilibrium between surface-connected and surface-dissociated caveolae is regulated by cavin3 and EHD2, where cavin3 promotes release and EHD2 constrains caveolae at the membrane.

DISCUSSION

The caveolae coat, which is built up of caveolins and cavins forming large assemblies, is thought to drive the biogenesis of caveolae, whereas peripherally associated proteins, such as EHD2 and pacsin2, control the stability and anchoring of caveolae (Parton and del Pozo, 2013). Caveolins appear to have an intrinsic ability to assemble in the membrane and the cavins are thought to control and fine-tune this oligomerisation. Recent work has proposed that cavin1 form cytosolic subcomplexes that associate with caveolins at a fixed 1:4 ratio (Gambin et al., 2014; Ludwig et al., 2013), but the precise stoichiometry of cavins within such subcomplexes, and how these are put together, is, however, not known. Here, we show that cavin3 is integrated in the coat through binding to cavin1 to reduce stability and promote rapid release of caveolae from the cell surface. We found that the N-terminal region of cavin3 interacts with the N-terminal region of cavin1 and that this facilitates the recruitment of cavin3 to caveolae. The cavin2 N-terminus also interacts with cavin1 but this region is, however, longer than the required region in cavin3 suggesting alterative modes for binding of cavin3 and cavin2. This region of the cavins share sequence homology and appear to be a common type of oligomerisation domain for forming cavin complexes. The N-terminal region of cavin1 was furthermore shown to be responsible for forming homotypic trimers of cavin1, as previously suggested for the full-length protein (Ludwig et al., 2013). These N-terminal trimers of cavin1 appear to have an extended shape and be the preferred assembly state of cavin1. We find that a trimer of cavin1 interacts with cavin3, which in our hands does not form homo-oligomers. This nicely correlates with the estimated 3:1 stoichiometry obtained by co-immunoprecipitation

experiments (Ludwig et al., 2013). Previous work shows that cavins form a stable sub-complex in the cytosol, composed of 9±2 cavins (Gambin et al., 2014). As previously proposed (Ludwig et al., 2013), we found that cavin3 competes with cavin2 for binding to cavin1 and that cavin2 and cavin3 themselves does not interact. Binding of cavin3 excludes cavin2 from the complex and we could not detect any evidence for intermixed subcomplexes. This competition might be due to the same binding site or binding to different structural arrangements of cavin1. It is reasonable to think that the local presence of cavin2 or cavin3 in the caveolae coat will influence the oligomerisation of caveolin1 differently and thereby the size, shape or dynamics of caveolae.

Using purified truncations of cavin3, we found that the middle domain of cavin3 binds to both membranes and to the scaffolding domain of caveolin1. This is the first time a direct interaction has been shown between cavins and caveolin. Cavin1 did not bind the scaffolding domain and it is likely that cavin1 rather interacts with specific oligomeric states of caveolin in the membrane. It has been questioned whether proteins that have been previously identified as interacting with scaffolding domain in fact do so, because the scaffolding region interacts with cholesterol and is in close proximity to the membrane, and might even be buried in the other leaflet of the membrane (Collins et al., 2012). However, we believe that because cavin3 is part of the caveolae coat and thereby locally concentrated, its affinity with the scaffolding region will affect caveolin in the lipid leaflet. The binding of cavin3 to caveolin1 is not required for biogenesis of caveolae because knockdown of cavin3 does not affect caveolae formation or shape and it is not required for recruitment of cavin3 to caveolae. This suggests that cavin3 instead has a regulatory role in the caveolae coat. Interestingly, membrane binding of cavin3 was sensitive to the cholesterol content, which implies that the interaction with the caveolin1 scaffolding domain might be regulated by the levels of cholesterol in caveolae. We found that the binding to caveolin1 was indeed cholesterol dependent given that removal of cholesterol increased the amount of cavin3 associated with caveolin1. We hypothesise that the scaffolding region of caveolin1 can be either buried in the membrane through its interaction with cholesterol or pulled out of the membrane through its interaction with cavin3. This will likely influence the membrane curvature initiated by caveolin1 and how it is positioned in the caveolae bulb. We found that the purified scaffolding domain of caveolin1 that bound to cavin3 formed oligomers, as previously described (Fernandez et al., 2002), although we do not think that this is a requirement for cavin3 binding. This shows that cavin3 can bind to caveolin1 although it is not oligomerised into the characteristic larger assemblies of caveolae, which is in agreement with previous work showing that cavin3 is associated with caveolae following scission and most tightly associated with caveolin1 (McMahon et al., 2009).

Our data predicts that although cavin1 binds higher order oligomers and drives the biogenesis of caveolae, cavin3 has a role in fine-tuning the caveolae coat. Using a novel approach we were able to measure the depth of caveolae in intact plasma membrane sheets and correlate this with direct imaging of fluorescently tagged proteins. (Dulhunty and Franzini-Armstrong, 1975; Lee and Schmid-Schönbein, 1995) We could observe a range of invaginations ranging from flat to highly invaginated caveolae. Interestingly, we found that cavin3 is enriched at more deeply invaginated caveolae but is not required for the formation of such structures. This suggests that cavin3 is preferentially recruited to mature caveolae bulbs, possibly through structural alterations in the oligomerisation of the caveolae coat that allows for cavin3 incorporation. Thus, cavin3 might play a regulatory role at the fully budded caveolae. The dynamics and fate of caveolae has to be coordinated with, and respond to, a diverse set of other cellular processes, which might explain the multiple faces of caveolae in terms of size, stability and trafficking. We set out to test whether cavin3 influenced the dynamics of caveolae by tracking caveolae using TIRF microscopy. As previously shown (Boucrot et al., 2011; Mundy et al., 2002; Pelkmans and Zerial, 2005), both the speed, duration time at the membrane and travelling distance varied greatly between caveolae. Although some caveolae were completely stable over time, others were flickering in what have been described as rounds of fission and fusion with the membrane. Interestingly, we found that in cells depleted of cavin3, the relative amount of very dynamic caveolae was significantly decreased, whereas the amount of highly stable caveolae was increased. Overexpression of cavin3 had the reverse effect showing that incorporation of cavin3 in the coat decreased the duration time of caveolae. However, in cells lacking EHD2, the relative amount of dynamic caveolae was greatly increased but could be rescued by re-expression of EHD2. This is in agreement with previous work showing that EHD2 constrains caveolae to the membrane (Morén et al., 2012). The stabilising effect in cells lacking cavin3 does not seem to be due to that it impedes the role of EHD2, given that we could not detect any apparent change in recruitment or stability of EHD2 at caveolae in cavin3-depleted cells. The interaction between cavin3 and the caveolin1 scaffolding domain appeared not to directly influence the caveolae stability because overexpression of a deletion mutant could also rescue the cavin3 depletion effect. This suggests that other regions of cavin3 are involved or that the presence of cavin3 in the caveolae coat exclude other stabilising components. Our results propose that cavin3 and EHD2 control the equilibrium between caveolae that are stably associated with the cell surface and kiss-and-run type of caveolae, which undergo rounds of fission and fusion. The background and mechanisms behind the kiss-and-run phenomenon of caveolae is largely unknown, but it might serve as a surface-buffering system for control of membrane tension, lipid homeostasis or signalling. Cavin3 has, similar to caveolin and caveolae, been heavily implicated in various types of cancer where it appears to act as a tumour suppressor (Bai et al., 2012; Xu et al., 2001). Although the precise role that cavin3 plays to prevent cancer development is not known, the proposed function as a positive regulator of caveolae dynamics might explain its impact on human health.

MATERIALS AND METHODS

DNA constructs, antibodies and reagents

DNA inserts were PCR amplified with flanking restriction sites and cloned into pET24d or pGEX4T2 for bacterial expression or pCMVmyc, pmCherry-C1, pmCherry-N1 or pmKO1-MC1 for expression in mammalian cells. N-terminal GFP-tagged cavin2 and cavin3 as well as C-terminal GFP-tagged cavin1 was a kind gift from Robert G. Parton, University of Queensland, Australia. Rabbit anti-EHD2 and rabbit anti-cavin3 were generated and affinity-purified using recombinant EHD2 or cavin3 respectively. Commercially acquired antibodies included mouse anti-clathrin heavy chain (BD Biosciences), rabbit anti-RFP (A00682, GenScript) and mouse anti-GFP (A11120, Invitrogen), rabbit anti-Caveolin-1 (ab2910), rabbit anti-PTRF (ab48824), rabbit anti-PRKCDBP (ab83913), goat anti-PRKCDBP (ab99427) and mouse anti-Thioredoxin (ab139677) from Abcam. Secondary antibody conjugated to Alexa Fluor 568 (Molecular Probes), horseradish peroxidase (HRP; Sigma-Aldrich and Agrisera) were used for immunofluorescence and western blot

detections. Stealth technology siRNA was purchased from Invitrogen. Human cavin3 siRNAa, 5′-GGAAGCUCCACGUUCUGCUCUUCAA-3′; human cavin3 siRNA, 5′-CCGAAGAAGCUCUGCUCCAAAUG-GA-3′; human EHD2 siRNA, 5′-UCCGCAAACUCAACCCUUUCGG-AAA-3′; and human caveolin1, 5′-CCCACUCUUUGAAGCUGUUGG-GAAA-3′.

Protein purification and pulldown assays

Proteins were expressed as either N-terminal His_6–Trx, His_6–MBP or GST fusion proteins in *E. coli* Rosetta pLysS strain using auto-induction LB medium (Studier, 2005) essentially as previously described (Pylypenko et al., 2007). Imidazole and glutathione was removed by gel filtration with parallel exchange of protein in 25 mM HEPES buffer pH 7.4 with 300 mM NaCl. The His_6 and GST fusion tags were removed by TEV protease or thrombin, respectively followed by affinity purification. For pulldown assays, the Glutathione–Sepharose-4B bead-bound GST fusion protein (bait) was incubated with Trx-tagged or untagged protein at a 3:1 M ratio, in binding buffer (25 mM HEPES buffer pH 7.4, 300 mM NaCl) at gentle agitation for 2 h at 6℃ before addition of glutathione–Sepharose-4B and further incubation for 40 min to bind the bait protein. Beads were sedimented by centrifugation at 2000 ***g*** for 2 min and 90% of the supernatant was removed. For rapid separation of beads from unbound molecules, the tubes were placed upside down in 1.5 ml Eppendorf tubes containing binding buffer and centrifuged at 20,000 ***g*** for 30 s. The sedimented beads were washed twice in binding buffer supplemented with 0.1% Triton X-100 and once in binding buffer. The sample was eluted by boiling in SDS sample buffer and analysed by SDS-PAGE and immunoblotting. Each pulldown experiment was repeated three times with the same results.

Immunoprecipitation

Flp-In TRex HeLa cells expressing caveolin1–GFP and HeLa cells overexpressing cavin1–GFP plus mCherry–cavin3 or cavin1–GFP and mCherry–cavin3-83–260 were grown in 9-cm tissue culture dishes until confluence. Cholesterol depletion was achieved by treating cells with 10 mM MβCD for 1 h at 37℃. Cells were washed extensively in cold PBS and incubated on ice. 1 ml of cold 25 mM HEPES pH 7.4, 150 mM NaCl buffer containing 1% Triton X-100, protease inhibitor cocktail (set III, Calbiochem) and phosphatase inhibitors was added to each plate and scraped cells were resuspended well for full lysis on ice, the non-nuclear fraction was separated by centrifugation at 1100 ***g*** for 5 min. The supernatant was incubated with 10 µl of GFP-Trap_A beads for 2 h, on a roller with gentle agitation at 6℃. The beads were sedimented and washed extensively with lysis buffer, boiled in SDS sample buffer. The eluted material was analysed by SDS-PAGE and western blotting.

Liposome-binding assay

Total brain lipids (Folch fraction) (Sigma) mixed in chloroform with methanol was dried under a stream of nitrogen and resuspended in 25 mM HEPES buffer (pH 7.4, 150 mM NaCl) and sonicated to generate spherical liposomes. For titration of cholesterol levels, the Folch fraction was dosed with the corresponding amount of cholesterol (5% and 10%) to give a final concentration of 1 mg/ml. Full-length and different truncated forms of cavin1 and cavin3 (1 µM) were incubated together with liposomes for 10 min at room temperature. The samples were centrifuged at 100,000 ***g*** for 20 min, and the supernatant and pellet were analysed by SDS-PAGE and Coomassie staining.

GEMMA and gel filtration analysis

Trx–cavin1-1–100 and Trx–cavin3-1–84 present in 25 mM HEPES buffer pH 7.4, 300 mM NaCl were exchanged into 100 mM ammonium acetate buffer, pH 7.6 by gel filtration chromatography to remove non-volatile salts. The proteins were diluted in the range of 0.01–0.1 mg/ml in 20 mM ammonium acetate buffer, pH 7.6 containing 0.005% Tween 20. The GEMMA system consists of the following components: a 3480 electrospray aerosol generator, a 3080 electrostatic classifier, a 3085 differential mobility analyzer and a 3025A ultrafine condensation particle counter (TSI Corp., Shoreview, MN). Most of the parameters were used according to manufacturer's suggestion, to get a stable signal every sample was scanned five times at 1.7 psi. The proteins were scanned at the size range of 2.5–25.0 nm for 105 s/scan, and molecular mass was calculated by using a particle density of 0.58 g/cm^3. The averages of 20 different standard proteins ranging in size from 15–900 kDa were used to estimate particle density. The Stokes radius (Rs) of purified Trx-cavin1 1–100 was estimated by gel filtration chromatography on a Superdex 200 column with the ÄKTA purifier fast protein liquid chromatography system (Amersham Pharmacia Biotech). The protein was eluted with 25 mM HEPES buffer pH 7.4, 300 mM NaCl and column was calibrated with standard proteins of known Stokes radii (cytochrome *c*, 1.70 nm; ovalbumin, 3.05 nm; BSA, 3.55 nm; aldolase, 4.81 nm; catalase, 5.20 nm; ferritin, 6.10 nm). The molecular mass of the oligomers was estimated based on the Stokes radius.

Crosslinking

Glutaraldehyde (25%) (Scharlau) was diluted in MQ water to the desired concentration. 45 µl of 3 µM Trx–cavin1-1–100 was titrated with 5 µl glutaraldehyde solution at room temperature for 5 min (final concentrations 0.2–0.001%). For study of the heterocomplexes, 3 µM of either Trx–cavin1-1–100 or Trx–cavin3-1–65 was titrated against increasing amounts of Trx–cavin3-1–65, Trx–cavin3-1–135 or Trx–cavin1–1–100. The protein samples were mixed well and incubated at room temperature for 10 min before crosslinking with 0.05% glutaraldehyde. The reaction was stopped by addition of 5 µl of 7% sodium borhydride (Merck) dissolved in 100 mM NaOH or 1 M Tris-HCl (pH 8.0). Control samples were treated with 1% SDS before treating with glutaraldehyde. Crosslinked protein samples were mixed with 6×SDS sample buffer and the oligomers were examined by SDS-PAGE and Coomassie staining.

Dynamic light scattering

Protein samples were analysed using a Zetasizer Nano (Malvern, Malvern, UK) instrument (measuring scattered light at 173˚, 630 nm light source). 70 µl samples at 0.5 mg/ml were measured in a BRAND UV cuvettes (Sigma-Aldrich), each sample was measured 5 times for 120 s, using the Stokes–Einstein equation; the autocorrelation curves were fitted with software provided by the instrument manufacturer.

AFM intensity correlation

Unroofing of cells was performed by adapting protocols devised previously (Heuser, 1989; Heuser and Anderson, 1989; Usukura et al., 2012). Cells were treated for ~10 s with buffer (70 mM KCl, 30 mM HEPES, 5 mM $MgCl_2$, 3 mM EDTA) supplemented with 0.3 mg/ml poly-lysin, transferred to 1:2 hypotonic solution (buffer:H_2O) and then changed back to regular buffer before sonication. The sample was sonicated using a probe sonicator for 1 s about half a cm above sample surface. The sample was fixed directly using 3%:0.5% PFA:glutaraldehyde solution for 30 min at room temperature. AFM measurements were performed using the Nanoscope software and a Bruker Bioscope Catalyst AFM unit and relevant probes. Scanasyst-Fluid and Scanasyst-Fluid+ probes were mainly used for measurement on unroofed samples. The AFM unit was placed on a Nikon Ti microscope, which enabled fluorescent imaging of the sample. AFM images were taken using the Bruker QNM mode and fluorescence images were acquired using an attached Nikon DS-Fi camera. Images were correlated using the Bruker miRO package and adjusted to match to the actin fluorescent signal. Image levels were adjusted using Photoshop and nanoscope to enable matching. Heights were measured within the nanoscope software, and fluorescence intensity was determined with ImageJ using an intensity plot profile across the centre of each spot, generating a parabola curve from which the intensity maxima was obtained. To normalise for intensity variation between sample preparations, the background was subtracted and the highest value was set to 100% to which each measurement in the sample was normalised. Normalised values were illustrated by a red-to-yellow scale using the Octave software.

Cell culture, siRNA knockdown and protein overexpression

HeLa cells (ATCC-CRM-CCL-2) were grown in DMEM medium (GIBCO) supplemented with 10% foetal bovine serum (Invitrogen). For generation of Flp-In TRex HeLa cell line, caveolin1 was amplified by PCR and cloned into a pcDNA5/FRT/TO vector modified to contain a C-terminal GFP tag and mutagenized to create the vector pcDNA5/FRT/TO/caveolin1-GFP by PCR cloning. The vector was cotransfected into Flp-In TRex tetracycline inducible HeLa cells (a kind gift from Stephen S. Taylor, University of Manchester, UK) with the Flp-recombinase-encoding plasmid pOG44 (Invitrogen) as described previously (Tighe et al., 2008). The cells were grown in DMEM (GIBCO) supplemented with 10% foetal bovine serum (Invitrogen), 100 µg/ml hygromycin B and 5 µg/ml blasticidin S HCl (both GIBCO) for plasmid selection. For transient transfection of cells, Lipofectamine 2000 (Invitrogen) was used according to manufacturer's instructions. Optimal knockdown was achieved after 4 to 5 days, as identified by SDS-PAGE and immunoblotting. For expression of constructs containing caveolin1, cavin1, cavin2, cavin3 or EHD2, cells were transfected 16 to 24 h prior to the experiment.

Fixed- and live-cell imaging

HeLa cells and Flp-In TRex HeLa cells were fixed in 3% paraformaldehyde in PBS for 15 min at room temperature, then washed in PBS. For immunofluorescence analysis, cells were blocked in 5% goat serum with 0.05% saponin in PBS before staining with the appropriate antibodies in 1% goat serum, 0.05% saponin in PBS using standard protocols. Images of fixed cell samples were captured using an A1 R Laser Scanning Confocal Microscope system (ANDOR iXon EMCCD camera) (Nikon Instruments) under control of the NIS-Elements Microscope Imaging Software and a 60× lens (Apochromat 1.40 Oil λS 0.17 WD 0.14, Nikon), at the appropriate excitation and emission wavelengths. For live-cell imaging, cells were grown and transfected according to standard protocols on uncoated MatTek dishes. Live-cell experiments were conducted using a growth chamber (37℃, 5% CO_2) in connection to the Nikon system, allowing real-time TIRF acquisitions with a 100× lens (Apochromat 1.49 Oil 0.13–0.20 DIC N2, Nikon). For FRAP experiments, the region of interest was photobleached for 10 s using a 561 laser. Single images were taken every 30 s after photobleaching, and recovery intensity was measured for a total of 15 min. The representative microscopic images shown in the figures were prepared (cropped, rotated and linearly adjusted for intensity) using Adobe Photoshop CS5.

Image and statistical analysis

The dynamics of caveolin1–GFP structures after siRNA transfection were evaluated by analysing TIRF live-cell acquisitions (3 s between frames, over 5 min) using the Imaris Software V7.5 (Bitplane) tracking mode (estimated diameter=0.4 µm, background subtraction, Brownian motion, maximum distance=0.8 µm, maximum gap size=4, no fill gap, track duration above). For TIRF live-cell acquisitions of cells expressing mCherry–cavin2 or mCherry–cavin3, only mCherry-positive structures colocalizing with caveolin1–GFP were evaluated using the same tools and settings as above. Statistical analyses were performed using GraphPad Prism.

Acknowledgements

The authors would like to thank the Biochemical Imaging Centre Umeå, Venkateswara Jonna and Anders Hofer for help with GEMMA analysis and Rob Parton for sending constructs.

Competing interests

The authors declare no competing or financial interests.

Author contributions

J.M., B.M, E.L., and R.L. designed and performed experiments. M.R.H. generated cellular tools and performed experiments. J.M and R.L. wrote the manuscript. All authors commented on the final manuscript.

Funding

This work was supported by the Swedish Cancer Society; the Swedish Research Council; Swedish Foundation for Strategic Research; the Kempe foundation; and Molecular Infection Medicine Sweden (MIMS). Deposited in PMC for immediate release.

Supplementary material

Supplementary material available online at
http://jcs.biologists.org/lookup/suppl/doi:10.1242/jcs.161463/-/DC1

References

Bai, L., Deng, X., Li, Q., Wang, M., An, W., Deli, A., Gao, Z., Xie, Y., Dai, Y. and Cong, Y. S. (2012). Down-regulation of the cavin family proteins in breast cancer. *J. Cell. Biochem.* **113**, 322-328.

Bastiani, M. and Parton, R. G. (2010). Caveolae at a glance. *J. Cell Sci.* **123**, 3831-3836.

Bastiani, M., Liu, L., Hill, M. M., Jedrychowski, M. P., Nixon, S. J., Lo, H. P., Abankwa, D., Luetterforst, R., Fernandez-Rojo, M., Breen, M. R. et al. (2009). MURC/Cavin-4 and cavin family members form tissue-specific caveolar complexes. *J. Cell Biol.* **185**, 1259-1273.

Boucrot, E., Howes, M. T., Kirchhausen, T. and Parton, R. G. (2011). Redistribution of caveolae during mitosis. *J. Cell Sci.* **124**, 1965-1972.

Breen, M. R., Camps, M., Carvalho-Simoes, F., Zorzano, A. and Pilch, P. F. (2012). Cholesterol depletion in adipocytes causes caveolae collapse concomitant with proteosomal degradation of cavin-2 in a switch-like fashion. *PLoS ONE* **7**, e34516.

Byrne, D. P., Dart, C. and Rigden, D. J. (2012). Evaluating caveolin interactions: do proteins interact with the caveolin scaffolding domain through a widespread aromatic residue-rich motif? *PLoS ONE* **7**, e44879.

Collins, B. M., Davis, M. J., Hancock, J. F. and Parton, R. G. (2012). Structure-based reassessment of the caveolin signaling model: do caveolae regulate signaling through caveolin-protein interactions? *Dev. Cell* **23**, 11-20.

Dulhunty, A. F. and Franzini-Armstrong, C. (1975). The relative contributions of the folds and caveolae to the surface membrane of frog skeletal muscle fibres at different sarcomere lengths. *J. Physiol.* **250**, 513-539.

Fernandez, I., Ying, Y., Albanesi, J. and Anderson, R. G. (2002). Mechanism of caveolin filament assembly. *Proc. Natl. Acad. Sci. USA* **99**, 11193-11198.

Fujita, A., Cheng, J., Tauchi-Sato, K., Takenawa, T. and Fujimoto, T. (2009). A distinct pool of phosphatidylinositol 4,5-bisphosphate in caveolae revealed by a nanoscale labeling technique. *Proc. Natl. Acad. Sci. USA* **106**, 9256-9261.

Gambin, Y., Ariotti, N., McMahon, K. A., Bastiani, M., Sierecki, E., Kovtun, O., Polinkovsky, M. E., Magenau, A., Jung, W., Okano, S. et al. (2014). Single-molecule analysis reveals self assembly and nanoscale segregation of two distinct cavin subcomplexes on caveolae. *eLife* **3**, e01434.

Hansen, C. G., Bright, N. A., Howard, G. and Nichols, B. J. (2009). SDPR induces membrane curvature and functions in the formation of caveolae. *Nat. Cell Biol.* **11**, 807-814.

Hansen, C. G., Shvets, E., Howard, G., Riento, K. and Nichols, B. J. (2013). Deletion of cavin genes reveals tissue-specific mechanisms for morphogenesis of endothelial caveolae. *Nat. Commun.* **4**, 1831.

Hayer, A., Stoeber, M., Bissig, C. and Helenius, A. (2010). Biogenesis of caveolae: stepwise assembly of large caveolin and cavin complexes. *Traffic* **11**, 361-382.

Heuser, J. (1989). Effects of cytoplasmic acidification on clathrin lattice morphology. *J. Cell Biol.* **108**, 401-411.

Heuser, J. E. and Anderson, R. G. (1989). Hypertonic media inhibit receptor-mediated endocytosis by blocking clathrin-coated pit formation. *J. Cell Biol.* **108**, 389-400.

Hill, M. M., Bastiani, M., Luetterforst, R., Kirkham, M., Kirkham, A., Nixon, S. J., Walser, P., Abankwa, D., Oorschot, V. M., Martin, S. et al. (2008). PTRF-Cavin, a conserved cytoplasmic protein required for caveola formation and function. *Cell* **132**, 113-124.

Lee, J. and Schmid-Schönbein, G. W. (1995). Biomechanics of skeletal muscle capillaries: hemodynamic resistance, endothelial distensibility, and pseudopod formation. *Ann. Biomed. Eng.* **23**, 226-246.

Liu, L., Brown, D., McKee, M., Lebrasseur, N. K., Yang, D., Albrecht, K. H., Ravid, K. and Pilch, P. F. (2008). Deletion of Cavin/PTRF causes global loss of caveolae, dyslipidemia, and glucose intolerance. *Cell Metab.* **8**, 310-317.

Liu, L., Hansen, C. G., Honeyman, B. J., Nichols, B. J. and Pilch, P. F. (2014). Cavin-3 knockout mice show that cavin-3 is not essential for caveolae formation, for maintenance of body composition, or for glucose tolerance. *PLoS ONE* **9**, e102935.

Ludwig, A., Howard, G., Mendoza-Topaz, C., Deerinck, T., Mackey, M., Sandin, S., Ellisman, M. H. and Nichols, B. J. (2013). Molecular composition and ultrastructure of the caveolar coat complex. *PLoS Biol.* **11**, e1001640.

McMahon, K. A., Zajicek, H., Li, W. P., Peyton, M. J., Minna, J. D., Hernandez, V. J., Luby-Phelps, K. and Anderson, R. G. (2009). SRBC/cavin-3 is a caveolin adapter protein that regulates caveolae function. *EMBO J.* **28**, 1001-1015.

Morén, B., Shah, C., Howes, M. T., Schieber, N. L., McMahon, H. T., Parton, R. G., Daumke, O. and Lundmark, R. (2012). EHD2 regulates caveolar dynamics via ATP-driven targeting and oligomerization. *Mol. Biol. Cell* **23**, 1316-1329.

Mundy, D. I., Machleidt, T., Ying, Y. S., Anderson, R. G. and Bloom, G. S. (2002). Dual control of caveolar membrane traffic by microtubules and the actin cytoskeleton. *J. Cell Sci.* **115**, 4327-4339.

Murata, M., Peränen, J., Schreiner, R., Wieland, F., Kurzchalia, T. V. and Simons, K. (1995). VIP21/caveolin is a cholesterol-binding protein. *Proc. Natl. Acad. Sci. USA* **92**, 10339-10343.

Nassoy, P. and Lamaze, C. (2012). Stressing caveolae new role in cell mechanics. *Trends Cell Biol.* **22**, 381-389.

Park, H., Go, Y. M., Darji, R., Choi, J. W., Lisanti, M. P., Maland, M. C. and Jo, H. (2000). Caveolin-1 regulates shear stress-dependent activation of extracellular signal-regulated kinase. *Am. J. Physiol.* **278**, H1285-H1293.

Parton, R. G. and del Pozo, M. A. (2013). Caveolae as plasma membrane sensors, protectors and organizers. *Nat. Rev. Mol. Cell Biol.* **14**, 98-112.

Pelkmans, L. and Zerial, M. (2005). Kinase-regulated quantal assemblies and kiss-and-run recycling of caveolae. *Nature* **436**, 128-133.

Pelkmans, L., Fava, E., Grabner, H., Hannus, M., Habermann, B., Krausz, E. and Zerial, M. (2005). Genome-wide analysis of human kinases in clathrin- and caveolae/raft-mediated endocytosis. *Nature* **436**, 78-86.

Pylypenko, O., Lundmark, R., Rasmuson, E., Carlsson, S. R. and Rak, A. (2007). The PX-BAR membrane-remodeling unit of sorting nexin 9. *EMBO J.* **26**, 4788-4800.

Razani, B. and Lisanti, M. P. (2001). Caveolin-deficient mice: insights into caveolar function human disease. *J. Clin. Invest.* **108**, 1553-1561.

Razani, B., Woodman, S. E. and Lisanti, M. P. (2002). Caveolae: from cell biology to animal physiology. *Pharmacol. Rev.* **54**, 431-467.

Rothberg, K. G., Heuser, J. E., Donzell, W. C., Ying, Y. S., Glenney, J. R. and Anderson, R. G. (1992). Caveolin, a protein component of caveolae membrane coats. *Cell* **68**, 673-682.

Shvets, E., Ludwig, A. and Nichols, B. J. (2014). News from the caves: update on the structure and function of caveolae. *Curr. Opin. Cell Biol.* **29**, 99-106.

Sinha, B., Köster, D., Ruez, R., Gonnord, P., Bastiani, M., Abankwa, D., Stan, R. V., Butler-Browne, G., Vedie, B., Johannes, L. et al. (2011). Cells respond to mechanical stress by rapid disassembly of caveolae. *Cell* **144**, 402-413.

Stoeber, M., Stoeck, I. K., Hänni, C., Bleck, C. K., Balistreri, G. and Helenius, A. (2012). Oligomers of the ATPase EHD2 confine caveolae to the plasma membrane through association with actin. *EMBO J.* **31**, 2350-2364.

Studier, F. W. (2005). Protein production by auto-induction in high density shaking cultures. *Protein Expr. Purif.* **41**, 207-234.

Tighe, A., Staples, O. and Taylor, S. (2008). Mps1 kinase activity restrains anaphase during an unperturbed mitosis and targets Mad2 to kinetochores. *J. Cell Biol.* **181**, 893-901.

Usukura, J., Yoshimura, A., Minakata, S., Youn, D., Ahn, J. and Cho, S. J. (2012). Use of the unroofing technique for atomic force microscopic imaging of the intra-cellular cytoskeleton under aqueous conditions. *J. Electron Microsc. (Tokyo)* **61**, 321-326.

Wikman, H., Sielaff-Frimpong, B., Kropidlowski, J., Witzel, I., Milde-Langosch, K., Sauter, G., Westphal, M., Lamszus, K. and Pantel, K. (2012). Clinical relevance of loss of 11p15 in primary and metastatic breast cancer: association with loss of PRKCDBP expression in brain metastases. *PLoS ONE* **7**, e47537.

Williams, T. M. and Lisanti, M. P. (2004). The caveolin proteins. *Genome Biol.* **5**, 214.

Xu, X. L., Wu, L. C., Du, F., Davis, A., Peyton, M., Tomizawa, Y., Maitra, A., Tomlinson, G., Gazdar, A. F., Weissman, B. E. et al. (2001). Inactivation of human SRBC, located within the 11p15.5-p15.4 tumor suppressor region, in breast and lung cancers. *Cancer Res.* **61**, 7943-7949.